# Interfacial Charge Separation in $ZrO_2$-Coupled Bismuth Sulfobromide Photocatalysts for $CO_2$-to-$CH_4$ Conversion

**Authors**

Liam Anderson[1], Sophie Bennett[2], Daniel Foster[3*]

**Affiliations**

School of Materials Science and Engineering, Faculty of Science, UNSW Sydney, Sydney, NSW 2052, Australia

***Corresponding author:** Daniel.Foster@unsw.edu.au

**Abstract**

Photocatalytic $CO_2$ reduction requires efficient charge separation and suitable surface sites for multi-electron transfer. Herein, $ZrO_2$-coupled bismuth sulfobromide heterojunctions were synthesized through a solvothermal method and applied to gas-phase $CO_2$ photoreduction. XRD, TEM, XPS, UV–vis diffuse reflectance spectroscopy, photoluminescence, and transient photocurrent measurements confirmed the formation of a strongly coupled interface between $ZrO_2$ and bismuth sulfobromide. The optimized heterojunction exhibited a $CH_4$ evolution rate of 28.7 μmol $g^{-1}$ $h^{-1}$, which was 3.4 times higher than that of pristine bismuth sulfobromide. Isotope labeling with $^{13}CO_2$ confirmed that methane originated from $CO_2$ reduction rather than surface carbon contamination. The enhanced activity was attributed to improved electron transfer from the sulfobromide phase to $ZrO_2$ and increased stabilization of $CO_2$-derived intermediates at interfacial oxygen sites.

**Keywords:** $CO_2$ photoreduction; methane production; $ZrO_2$ heterojunction; bismuth sulfobromide; charge separation; photocatalysis

## 1. Introduction

Photocatalytic $CO_2$ conversion provides a promising approach for coupling solar-energy utilization with carbon recycling by transforming $CO_2$ into energy-rich chemicals and fuels. Among the possible reduction products, $CH_4$ is particularly attractive because of its high energy density, compatibility with existing natural-gas infrastructure, and potential for long-term chemical energy storage. Nevertheless, selective $CO_2$ photoreduction to $CH_4$ remains challenging because the overall process involves eight-electron transfer together with multiple protonation and C–O bond-cleavage steps. These elementary processes compete with kinetically simpler pathways leading to CO, $H_2$, formate, and methanol. In addition, the chemical stability of $CO_2$, rapid recombination of photogenerated electrons and holes, insufficient visible-light utilization, and sluggish surface reaction kinetics collectively limit the rate of deep reduction to methane. Recent studies have therefore focused on heterojunction construction, defect engineering, cocatalyst deposition, and surface modification to improve both charge-carrier utilization and surface

reaction kinetics [1,2]. These results demonstrate that increasing the lifetime or density of photogenerated electrons alone is insufficient to achieve high $CH_4$ selectivity. Efficient photocatalysts must simultaneously provide suitable adsorption configurations for $CO_2$, stabilize key carbon-containing intermediates, and sustain sequential proton-coupled electron-transfer steps. Although developed for thermocatalytic $CO_2$ hydrogenation rather than photocatalysis, recent ensemble modeling of structurally diverse inverse $ZrO_2$/Cu interfaces showed that variations in local interfacial configuration can substantially alter reaction mechanisms, intrinsic reactivity, and deactivation behavior [3]. This observation emphasizes a broader principle relevant to photocatalytic systems: the catalytic function of $ZrO_2$-containing interfaces cannot be understood solely from their nominal composition, because local coordination and interfacial electronic structure may strongly influence the stabilization and conversion of $CO_2$-derived intermediates. Similar relationships between interfacial charge transfer, intermediate adsorption, and product selectivity have been observed in $In_2S_3/In_2O_3$, Cu–$TiO_2/WO_3$, and $CuInSnS_4$ photocatalytic systems [4,5].

Bismuth-based semiconductors have attracted extensive interest for photocatalytic $CO_2$ reduction because their electronic structures, optical absorption, and surface chemistry can be regulated through anion composition, vacancy formation, and heterointerface construction. Considerable attention has been given to BiOBr, BiOCl, and related bismuth oxyhalides, whose layered structures facilitate the formation of internal electric fields and provide opportunities for defect-mediated charge separation. Vacancy-rich BiOBr, $WO_3$/BiOBr, g-$C_3N_4$/BiOBr, and Bi–BiOCl/$TiO_2$ systems have exhibited improved carrier separation and enhanced $CO_2$ photoconversion compared with the corresponding individual components [6,7]. However, improved overall conversion does not necessarily result in efficient methane formation. Many bismuth-based photocatalysts predominantly generate CO, formate, or methanol because these products require fewer electron-transfer and protonation events, whereas $CH_4$ formation demands prolonged retention of carbon intermediates on the catalyst surface and continuous delivery of reducing equivalents. Premature desorption of CO or insufficient stabilization of highly reduced intermediates can therefore terminate the reaction before complete reduction to methane [8,9]. Consequently, designing a photocatalyst for selective $CH_4$ generation requires not only favorable band alignment and rapid interfacial charge separation but also surface sites capable of promoting successive hydrogenation and C–O bond cleavage. $ZrO_2$ offers several properties that make it a potentially useful interfacial component in such systems. It is chemically and thermally stable and contains Lewis acidic Zr centers and surface oxygen species that can participate in $CO_2$ adsorption and activation. Surface hydroxyl groups, coordinatively unsaturated Zr sites, and oxygen-deficient environments may alter the adsorption geometry and electronic state of $CO_2$-derived species [10,11]. Nevertheless, bulk $ZrO_2$ possesses a wide band gap, weak visible-light absorption, and relatively poor charge transport, which restrict its use as an independent visible-light photocatalyst. $ZrO_2$ is therefore more commonly introduced as a surface modifier, electron-accepting component,

adsorption-enhancing phase, or heterojunction partner. Studies involving Pt/$ZrO_2$, Mn/$ZrO_2$, and $ZrO_2$/ZnS have shown that coupling $ZrO_2$ with catalytically or photoactively complementary phases can enhance $CO_2$ adsorption, modify interfacial electron transport, and promote methane formation [12,13]. These findings suggest that the contribution of $ZrO_2$ extends beyond simple physical support. Properly constructed $ZrO_2$ interfaces may redistribute photogenerated charge, create additional adsorption environments, and modify the binding strength of carbon-containing intermediates. Such effects are especially relevant to methane formation because deep reduction requires that intermediates remain sufficiently stable to undergo successive proton-coupled electron-transfer reactions without being trapped irreversibly or released prematurely as partially reduced products. Bismuth sulfobromide represents another promising class of visible-light-responsive bismuth chalcohalide materials because the simultaneous presence of sulfide and bromide anions can produce electronic structures different from those of conventional bismuth oxyhalides. Its relatively strong visible-light response and adjustable band structure have stimulated investigations in photodetection, photovoltaic conversion, and photocatalytic pollutant degradation [14,15]. However, its potential for gas-phase $CO_2$ photoreduction, particularly for selective $CH_4$ formation, has received substantially less attention. This gap is important because gas-phase $CO_2$ conversion imposes requirements different from those encountered in pollutant degradation or liquid-phase photocatalysis. Charge carriers must reach accessible gas–solid interfacial sites, $CO_2$ and water-derived species must be adsorbed in suitable configurations, and carbon intermediates must undergo repeated electron and proton transfer without assistance from soluble sacrificial donors. Coupling bismuth sulfobromide with $ZrO_2$ may therefore provide complementary functions: the bismuth-containing semiconductor can serve as the principal visible-light absorber, whereas the $ZrO_2$-containing interface can regulate electron distribution and provide additional sites for adsorption and subsequent conversion of $CO_2$-derived intermediates. A properly formed heterointerface may also generate a directional driving force for charge migration, suppress bulk electron–hole recombination, and increase the probability that long-lived electrons participate in multi-electron surface reduction rather than being consumed through competing processes. Mechanistic evaluation of such heterojunction photocatalysts requires more than measurements of apparent product yield. Many reported $CO_2$ photoreduction studies are performed in liquid media containing sacrificial reagents, which can enhance carrier consumption but do not fully represent direct gas-phase conversion using $CO_2$ and water [16,17]. Reported catalytic rates are also difficult to compare because catalyst loading, irradiation intensity, spectral distribution, reactor volume, $CO_2$ pressure, humidity, reaction time, and product-normalization methods vary considerably among studies. More importantly, methane detection alone cannot unambiguously establish photocatalytic reduction of $CO_2$. Carbon-containing solvents, organic precursors, synthesis residues, adsorbed carbonate species, and adventitious surface contaminants may produce carbonaceous products under irradiation and lead to overestimation of genuine $CO_2$ conversion. Isotope labeling using $^{13}CO_2$ is therefore particularly valuable for verifying the carbon

origin of methane. Conventional photoluminescence and photocurrent measurements can provide evidence for altered recombination behavior and carrier transport, but they cannot independently establish the actual interfacial charge-transfer pathway or the chemical origin of enhanced selectivity. Their interpretation should be combined with crystallographic, microscopic, spectroscopic, and surface-chemical analyses to determine whether improvements originate from heterojunction formation, modified electronic states, increased light absorption, or changes in surface reaction sites [18,19].

Against this background, the present study develops $ZrO_2$-coupled bismuth sulfobromide heterojunctions through a solvothermal strategy and investigates their performance in direct gas-phase photocatalytic $CO_2$ reduction to $CH_4$. The material design is intended to integrate visible-light harvesting by the bismuth sulfobromide phase with the interfacial and surface functions provided by $ZrO_2$, thereby addressing charge recombination and sluggish deep-reduction kinetics within the same catalytic architecture. X-ray diffraction and transmission electron microscopy are used to determine phase composition, crystallinity, morphology, and interfacial contact, while X-ray photoelectron spectroscopy is employed to probe surface chemical states and changes in the local electronic environment associated with heterojunction formation. UV–vis diffuse reflectance spectroscopy, photoluminescence spectroscopy, and transient photocurrent measurements are combined to evaluate light absorption and photogenerated charge-carrier behavior. Particular emphasis is placed on connecting these electronic and structural characteristics with $CH_4$ formation rather than treating enhanced charge separation as an isolated performance descriptor. A $^{13}CO_2$ isotope-labeling experiment is further employed to verify that the detected methane originates from the supplied $CO_2$, providing direct evidence for the carbon-conversion pathway and excluding major contributions from residual carbon species. Through these complementary analyses, this study aims to clarify how the $ZrO_2$-containing interface alters charge separation, interfacial electron utilization, $CO_2$ adsorption, and the stabilization of intermediates required for sequential reduction toward $CH_4$. Establishing these relationships is expected to provide a mechanistic basis for understanding deep $CO_2$ photoreduction on bismuth-based heterojunctions and to offer a rational strategy for designing visible-light photocatalysts in which charge-transfer efficiency and surface multi-electron reaction kinetics are optimized simultaneously.

## 2. Materials and Methods

### 2.1. Catalyst Samples and Reaction Conditions

Six catalyst samples were prepared, including pure BiSBr, pure $ZrO_2$, and four $ZrO_2$/BiSBr composites containing 2, 5, 10, and 15 wt% $ZrO_2$. BiSBr was prepared from bismuth nitrate, thiourea, and potassium bromide by a solvothermal method. The mixed solution was placed in a Teflon-lined autoclave and heated at 160 °C for 12 h. The obtained solid was washed with ethanol and water and dried at 60 °C. $ZrO_2$ nanoparticles were added during synthesis to form direct

contact with BiSBr. Gas-phase $CO_2$ reduction was conducted in a 120 mL quartz reactor at room temperature and atmospheric pressure. For each test, 50 mg of catalyst was spread on a glass plate. Ultrapure water (5 mL) was placed at the bottom of the reactor to provide water vapour. The reactor was filled with high-purity $CO_2$ for 30 min before light exposure. A 300 W xenon lamp with a 420 nm cut-off filter was used. Each catalyst was tested three times, giving 18 independent tests.

### 2.2. Experimental Design and Control Tests

The four $ZrO_2$/BiSBr samples were compared with pure BiSBr and pure $ZrO_2$ under the same reaction conditions. The $ZrO_2$ content was changed to determine the amount needed for charge transfer without blocking visible-light absorption. A physical mixture of $ZrO_2$ and BiSBr was also tested. Its composition was the same as that of the best heterojunction sample. This control was used to separate the interface effect from simple particle mixing. Blank tests were carried out in the dark, without a catalyst, and under $N_2$ instead of $CO_2$. These tests were used to check thermal reactions, reactor contamination, and carbon products from surface residues. Before each test, the catalyst was heated at 100 °C under flowing $N_2$ for 1 h. This treatment removed weakly adsorbed carbon compounds. The stability of the best catalyst was tested over five cycles. Fresh $CO_2$ was added before each cycle.

### 2.3. Characterization and Quality Control

Crystal phases were identified by X-ray diffraction with Cu Kα radiation. Particle shape, lattice spacing, and interface contact were examined by transmission electron microscopy and high-resolution transmission electron microscopy. Surface elements and chemical states were measured by X-ray photoelectron spectroscopy. The C 1s peak at 284.8 eV was used for energy correction. Light absorption was measured by UV–vis diffuse reflectance spectroscopy. Charge recombination was studied by steady-state photoluminescence spectroscopy. Transient photocurrent was measured in a three-electrode cell under repeated light on–off cycles. Gas samples were collected every 30 min and analysed by gas chromatography. $CH_4$ was measured with a flame-ionization detector and a methanizer. CO and $H_2$ were measured with a thermal-conductivity detector. Calibration curves were prepared with certified gas standards before each test series. Blank injections were used to check background signals. The calibration error was kept below 3%. A test was repeated when the difference among three runs was greater than 5%. Signals detected in the dark, catalyst-free, or $N_2$ tests were removed from the final results.

### 2.4. Data Processing and Calculation Methods

Gas concentrations were converted into molar amounts using the reactor volume, temperature, and pressure. The $CH_4$ evolution rate was calculated as

$$r_{CH_4} = \frac{n_{CH_4}}{m_{cat} t},$$

where $r_{CH_4}$ is the $CH_4$ evolution rate in μmol $g^{-1}$ $h^{-1}$, $n_{CH_4}$ is the amount of $CH_4$ formed, $mcatm_{cat}mcat$ is the catalyst mass, and $t$ is the reaction time. The apparent quantum yield for $CH_4$ formation was calculated as

$$AQY(\%) = \frac{8N_{CH_4}}{N_{photon}} \times 100,$$

where $N_{CH_4}$ is the number of $CH_4$ molecules and $N_{photon}$ is the number of incident photons. The factor of eight represents the eight electrons needed to convert one $CO_2$ molecule into $CH_4$. Product formation rates were obtained from the slope of the concentration–time curves. Results were reported as mean values with standard deviations. Differences among catalyst groups were tested by one-way analysis of variance followed by Tukey's test. A value of $p<0.05$ was considered significant.

### 2.5. Isotope Tracing and Interface Analysis

The carbon source of $CH_4$ was checked using $^{13}CO_2$ under the same conditions as the normal photocatalytic tests. Gas products were measured by gas chromatography–mass spectrometry. The formation of $^{13}CH_4$ was confirmed by the signal at $m/z=17$. The signal at $m/z=16$ was also recorded to check carbon contamination. Surface reaction species were studied by in situ diffuse reflectance infrared Fourier-transform spectroscopy under $CO_2$ and water-vapour flow. Spectra were recorded before light exposure and at fixed reaction times. Changes in carbonate, bicarbonate, formate, and carbonyl bands were compared among pure BiSBr, the physical mixture, and the best $ZrO_2$/BiSBr sample. XPS shifts, photoluminescence intensity, and photocurrent density were examined together to determine the direction of electron transfer. These results were used to explain the relation among charge separation, oxygen-site adsorption, and $CH_4$ formation.

## 3. Results and Discussion

### 3.1. Phase Structure and Interface Formation

The XRD patterns confirmed the formation of pure BiSBr and $ZrO_2$ phases. Both sets of diffraction peaks were present in the $ZrO_2$/BiSBr samples, and no clear impurity peaks were observed. The weak $ZrO_2$ peaks at low loading were related to its small content and particle size. TEM images showed that $ZrO_2$ nanoparticles were evenly attached to the BiSBr surface rather than forming large separate particles. The HRTEM image in Fig. 1 showed clear lattice fringes from both phases and a close contact region at the interface. This contact provided a path for electron transfer between BiSBr and $ZrO_2$. The shifts in the Bi, S, Br, Zr, and O XPS peaks also indicated charge movement after coupling. Changes in the O 1s spectrum showed that oxygen-containing sites were present near the interface. These sites may improve $CO_2$ adsorption and help stabilize carbon-containing intermediates [20]. Wu et al. (2026) reported that BiSBr has

suitable band positions for $CO_2$ reduction, but rapid charge recombination can limit its activity. The $ZrO_2$/BiSBr interface reduced this problem by providing an additional electron-transfer path. Yang et al. (2026) also found that surface oxygen sites improved $CO_2$ adsorption and affected product formation during photocatalytic reduction.

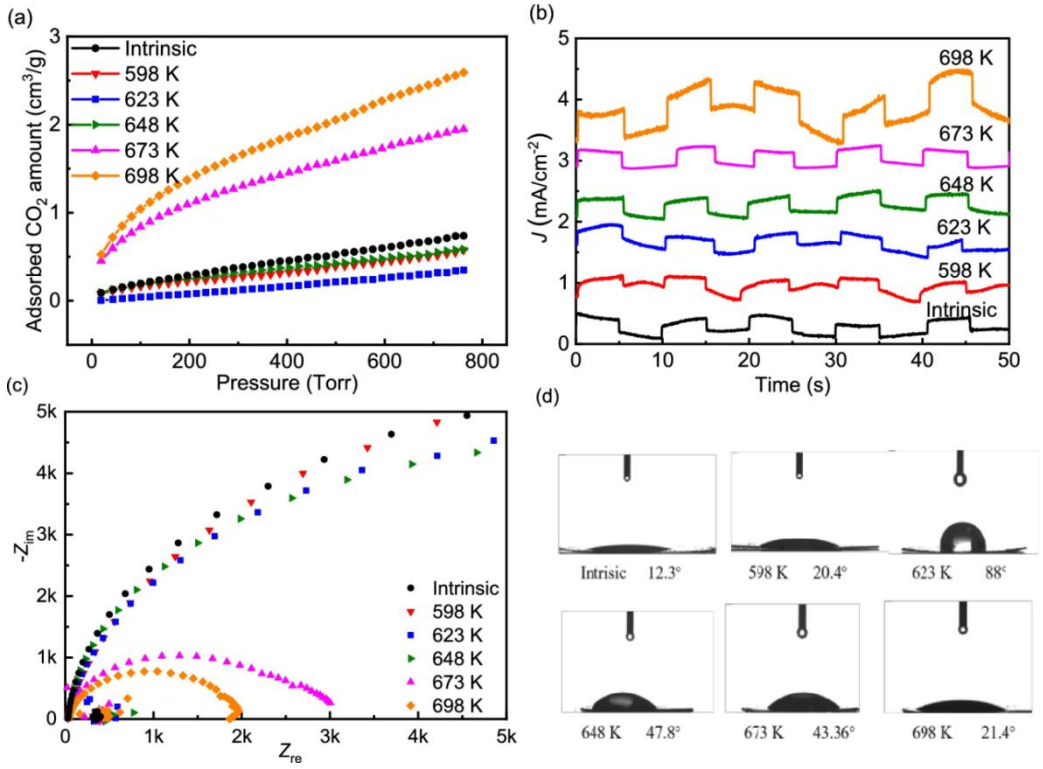


**Fig. 1.** Structure and charge transfer of BiSBr and $ZrO_2$/BiSBr photocatalysts.

### 3.2. Light Absorption and Charge Separation

Pure BiSBr showed strong absorption in the visible-light region, while $ZrO_2$ mainly absorbed ultraviolet light. The $ZrO_2$/BiSBr samples retained the visible-light response of BiSBr. However, high $ZrO_2$ loading caused a small decrease in light absorption because part of the BiSBr surface was covered. As shown in Fig. 1, the optimized sample had the lowest photoluminescence intensity and the highest transient photocurrent density. The lower photoluminescence signal showed that electron–hole recombination was reduced. The higher photocurrent response indicated that more photoexcited electrons reached the catalyst surface. These results support electron transfer from BiSBr to $ZrO_2$. BiSBr acted as the main light absorber, while $ZrO_2$ accepted electrons and supplied surface oxygen sites. This structure increased the number and lifetime of electrons available for $CO_2$ reduction. The effect depended on $ZrO_2$ loading. Low loading produced too few interface sites, whereas high loading blocked light absorption and active surface regions. Similar trends have been reported for $WO_3$/BiOBr and other bismuth-based heterojunctions, in which a moderate oxide content gave the best charge separation [21,22]. Wahba et al. (2026) also reported that fast electron transfer across several interfaces improved

$CO_2$ reduction. In comparison, the binary $ZrO_2$/BiSBr system provides a simpler structure for studying interface effects.

### 3.3. Photocatalytic $CO_2$-to-$CH_4$ Performance

Pure $ZrO_2$ showed little activity under visible light because of its wide band gap. Pure BiSBr produced $CH_4$ at a lower rate because many photoexcited charges recombined before reaching the surface. All $ZrO_2$/BiSBr samples showed higher $CH_4$ production than the two single materials. As shown in Fig. 2, the optimized heterojunction reached a $CH_4$ evolution rate of 28.7 μmol $g^{-1}$ $h^{-1}$, which was 3.4 times that of pure BiSBr. The physical mixture with the same composition showed lower activity than the solvothermally prepared sample. This result indicates that simple particle contact was not enough to improve $CH_4$ formation. A well-formed interface was needed for efficient electron transfer and surface reduction. The activity first increased and then decreased as the $ZrO_2$ content rose. The initial increase was caused by the formation of more interface sites. The later decrease resulted from surface coverage and weaker light absorption. No clear $CH_4$ signal was detected in the dark, without a catalyst, or under $N_2$. These tests ruled out thermal reactions and common carbon contamination. The optimized sample also retained most of its activity after five cycles. However, longer tests are still needed to confirm its stability. Al Zoub et al. (2026) reported that oxygen-rich surface sites promoted the conversion of $CO_2$ to $CH_4$ by improving reactant adsorption and electron use. The present results show that interfacial oxygen sites can produce a similar effect in $ZrO_2$/BiSBr.

### 3.4. Carbon Source and Reaction Pathway

The isotope test confirmed the carbon source of methane. Under normal $CO_2$, the main methane signal appeared at m/z=16. After $CO_2$ was replaced by $^{13}CO_2$, the main signal shifted to m/z=17, as shown in Fig. 2. This change confirmed that $CH_4$ was produced from $CO_2$ rather than from solvents, catalyst residues, or surface carbon. The in situ infrared spectra showed carbonate and bicarbonate bands after $CO_2$ entered the reactor. Formate and carbonyl-related bands became stronger during light exposure. These results suggest that $CO_2$ was first adsorbed on oxygen-containing sites and then reduced through several electron- and proton-transfer steps [23,24]. Under light irradiation, BiSBr generated electrons and holes. The electrons moved to $ZrO_2$ and took part in $CO_2$ reduction. The holes remained mainly in BiSBr and supported water oxidation. The $ZrO_2$ surface also helped retain $CO_2$-derived intermediates, which allowed further reduction to $CH_4$. Rana et al. (2025) linked stronger $CO_2$ and $H_2O$ adsorption with higher $CH_4$ production, while WU et al. (2026) used $^{13}CO_2$ tests to confirm the carbon source of methane. The present study combines these effects in one $ZrO_2$/BiSBr interface. However, the proposed pathway is mainly based on XPS, photocurrent, isotope, and infrared results. Operando EPR and X-ray absorption measurements are needed to identify short-lived intermediates and confirm the

electron-transfer route. Tests under natural sunlight and continuous-flow conditions are also needed before practical use.

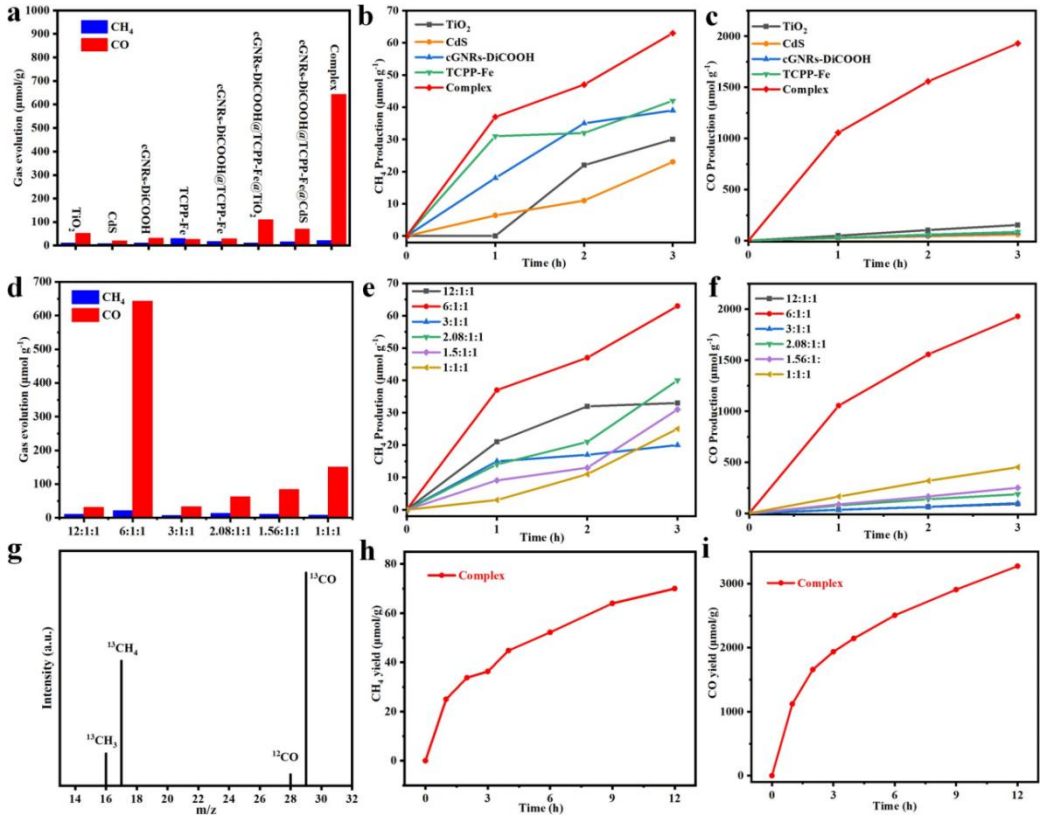


**Fig. 2.** $CO_2$-to-$CH_4$ activity and reaction pathway of the $ZrO_2$/BiSBr photocatalyst.

## 4. Conclusion

$ZrO_2$/BiSBr heterojunctions were prepared for gas-phase $CO_2$ reduction to $CH_4$. The best sample reached a $CH_4$ production rate of 28.7 μmol $g^{-1}$ $h^{-1}$, which was 3.4 times higher than that of pure BiSBr. Structural and surface analyses confirmed close contact between $ZrO_2$ and BiSBr. This interface reduced charge recombination and promoted electron transfer from BiSBr to $ZrO_2$. Oxygen sites on $ZrO_2$ also improved $CO_2$ adsorption and supported the formation of key reaction intermediates. The $^{13}CO_2$ test confirmed that $CH_4$ came from $CO_2$ rather than surface carbon residues. The main value of this study lies in combining interface charge transfer with surface oxygen sites to improve the multi-electron reduction of $CO_2$ to $CH_4$. The catalyst may be useful for solar-fuel production and gas-phase carbon conversion. However, the tests were carried out in a small batch reactor under controlled light. Longer stability tests, in situ measurements, natural-sunlight tests, and continuous-flow experiments are still needed to confirm the reaction process and practical performance.

## References

1. Jiao, Y., Shi, T., Zhao, B., & Wang, A. (2026). The Impact of VR Sketching Simulations on the Assessment of Scale and Site Suitability in Public Art Spaces.

2. Sarkar, D., Pramanik, J., Samajdar, S., Biswas, M., & Ghosh, S. (2025). Charge carrier dynamics in semiconductor–cocatalyst interfaces: influence on photocatalytic activities. RSC Applied Interfaces, 2(3), 573-598.
3. Yang, Z., Alexandrova, A. N., & Sautet, P. (2026). Modeling CO2 Hydrogenation to Methanol on an Ensemble of Inverse ZrO2 on Cu Catalytic Sites: Mechanism, Reactivity, and Deactivation. Angewandte Chemie, e5448247.
4. Liang, S., Zhang, X., Du, Y., & Chen, W. (2026). Supply Network Restructuring and Capacity Ramp-Up Limits in the Localized Expansion of High-Performance Computing Equipment Production. Available at SSRN 7339738.
5. Sebastián-Pascual, P., Herzog, A., Zhang, Y., Shao-Horn, Y., & Escudero-Escribano, M. (2025). Electrolyte effects in proton–electron transfer reactions and implications for renewable fuels and chemicals synthesis. Nature Catalysis, 8(10), 986-999.
6. Bao, Y., & Wang, H. (2026). Edge-to-Cloud Infrastructure Continuum: A Unified Framework for Optimizing Industrial IoT Systems. Available at SSRN 7185578.
7. Susikumar, T., Mohan, H., Kandasamy, M., Chakraborty, B., Shin, T., Navaneethan, M., & Jesuraj, P. J. (2025). Tailored S-scheme directed NiFe-LDH/Ag2S heterojunction for visible light-driven CO2 photoconversion. Applied Surface Science, 710, 163940.
8. Chen, F., Liang, H., Li, S., Yue, L., & Xu, P. (2025). Design of Domestic Chip Scheduling Architecture for Smart Grid Based on Edge Collaboration.
9. Park, S., Cho, J. H., Rhi, S., Hwang, S. J., Kang, J. H., Dong, W. J., & Kim, S. Y. (2026). Selective photocatalytic CO2 reduction to methane over CTAB stabilized two-dimensional CsPbBr3 nanosheets with gold cocatalysts. Nanoscale.
10. Liang, R., Feifan, F. N. U., Liang, Y., & Ye, Z. (2025). Emotion-Aware Interface Adaptation in Mobile Applications Based on Color Psychology and Multimodal User State Recognition. Frontiers in Artificial Intelligence Research, 2(1), 51-57.
11. López-Luque, I. (2025). Bifunctional and Nanospatial Effects in Copper Catalysts for Methanol Synthesis.
12. Du, Y. (2025). Research on Digital Quality Traceability System for Temperature-Controlled Supply Chain of Foreign Trade Wine Driven by Blockchain and IoT. Business and Social Sciences Proceedings, 4, 57-65.
13. Zitong, G., Jianliang, X., Ning, W., Junping, X., Shujuan, L., Qing, J., ... & Ke, S. (2026). Biochar as a multifunctional mediator enhances sulfate reduction of mine drainage in microbial electrolysis cells via direct interspecies electron transfer and microbial metabolic regulation. Journal of Environmental Chemical Engineering, 122840.
14. Jiao, Y., Zhao, B., Wang, A., & Shi, T. (2026). Construction and Empirical Study of a Modularized Teaching System for Art Courses Based on a Unified Training Pathway.
15. Rana, M. Z., Akter, S., Barik, A., Hasan, J., Islam, M. S., Ali, M. H., & Rahman, M. H. (2025). First-principles study of pressure-induced multifunctional response in RbYO2:

structural-mechanical stability, optoelectronic tunability, and photocatalytic performance enhancement. Results in Engineering, 27, 105934.

16. Bao, Y., Qiu, Y., & Wang, H. (2026, May). Unified Identity Layer for Hyperscale Ecosystems: A Framework for Cross-Platform User Attribution and Experimentation. In 2026 6th International Conference on Machine Learning and Intelligent Systems Engineering (MLISE) (pp. 540-543). IEEE.

17. Bertuletti, M., Fumagalli, A., Gramegna, A., Tommasi, M., Ramis, G., & Rossetti, I. (2026). Hole Scavenger Role during CO2 Photoreduction: Toward a New Hybrid Homogeneous/Heterogeneous Process. ACS Sustainable Chemistry & Engineering, 14(19), 9214-9228.

18. Chaerun, R. I., Astarini, N. A., Al Ittikhad, A., Syahputra, H. G., Winarko, R., & Chaerun, S. K. (2025). Characterization techniques in photocatalysis. In Photocatalytic hydrogen fuel generation: designing highly efficient semiconductor materials (pp. 251-314). Singapore: Springer Nature Singapore.

19. Yang, J. (2026). Stage-Coupled Computational Framework for Stratified Accessibility and Equity Analysis in Community-Based Elderly Care Services.

20. Wu, J., Wu, D., Zhang, J., & Peng, Y. (2026). Generative AI Feedback in Junior High School Artistic Creation Evaluation. Available at SSRN 7244838.

21. Wahba, M. A. (2026). Recent developments in metal oxide semiconductor photocatalysts for solar-driven environmental applications. Discover Materials, 6(1), 127.

22. Gu, X. (2026). Identifying Causal Effects and Analyzing Heterogeneity of User Growth Interventions on Digital Platforms: Evidence from Large-Scale Behavioral Data. Available at SSRN 6809181.

23. Al Zoubi, W., Al-hamdani, A. A. S., & Park, N. (2026). High-entropy alloy as efficient and stable catalysts for the CO2 and CO reductions. Materials Today Communications, 115676.

24. You, S. (2026). Verifiable Audit Mechanisms in AI Compliance Automation: Scalability. Available at SSRN 6547458.